



A criterion of dimensional design to improve flame spread resistance of magnesium alloy components

Bo HU¹, Jia-xuan HAN¹, De-jiang LI¹, Zi-xin LI¹, Xiao-qin ZENG¹,
Wen-jiang DING¹, Zhan-hong LIN², Chen JIN², Shou ZHAO²

1. National Engineering Research Center of Light Alloy Net Forming and the State Key Laboratory of Metal Matrix Composites, School of Materials Science and Engineering, Shanghai Jiao Tong University, Shanghai 200240, China;

2. Qinghai Salt Lake Tri-Magnesium Co., Ltd., Xining 810000, China

Received 1 October 2022; accepted 8 June 2023

Abstract: A criterion for predicting the flame spread time of stick-shaped Mg alloy samples was proposed based on the law of energy conservation. It is indicated that the flame spread time is mainly affected by the material and sample dimension. The initial temperature and ignition temperature of the control volume and the S/l_c ratio (the cross-sectional area/cross-sectional circumference) of the sample are decisive for the flame spread time. The flame spread time is proportional to the ΔH (the energy required to heat a unit mass of sample from initial temperature to ignition temperature) and the S/l_c ratio, which is confirmed in three Mg alloys of Mg–8.5Al–0.5Zn–0.2Mn, Mg–2.7Nd–0.4Zn–0.6Zr and Mg–4.0Y–3.3Nd–0.5Zr. For samples with the same dimension, the Mg–8.5Al–0.5Zn–0.2Mn alloy sample possesses the largest ΔH and the longest flame spread time. For samples with constant length and cross-sectional area, the sample with circular cross-section has the largest S/l_c ratio and the best flame spread resistance in the same alloy.

Key words: Mg alloy component; flame spread resistance; microstructure; dimensional design; criterion

1 Introduction

The demand for magnesium alloys in industry is increasing rapidly, due to their benefits of low density, high specific strength and good castability [1–4]. However, the application of Mg alloys in the aerospace is still limited by their flammable characteristics [5,6]. Conventional Mg alloys have a low ignition temperature and their combustion releases massive heat, resulting in rapid flame spread difficult to extinguish [7]. Although the Federal Aviation Administration (FAA) lifted the ban on the application of Mg alloys in aircraft cabins [8], which increases the possibility of

applying Mg alloy components in the aerospace, the safety is still a top concern. The primary way to eliminate this unsafety is to increase ignition temperature and flame spread resistance through the fire-resistant design of Mg alloy components.

Alloying is an effective way to increase the ignition temperature of Mg alloys. The ignition temperature can be increased by optimizing the alloy microstructure, especially the secondary phase. Commercial AZ series Mg alloys have low ignition temperatures due to the presence of the low melting point Mg₁₇Al₁₂ phase, such as AZ80 (known as ZM5 in China) at approximately 540 °C [9]. CHENG et al [10] added 0.8 wt.% Ca to the ZM5 alloy to replace some Mg₁₇Al₁₂ with high melting

Corresponding author: De-jiang LI, Tel: +86-21-54742381, E-mail: lidedjiang@sjtu.edu.cn;

Xiao-qin ZENG, Tel: +86-21-54742301, E-mail: xqzeng@sjtu.edu.cn

DOI: 10.1016/S1003-6326(23)66458-1

1003-6326/© 2024 The Nonferrous Metals Society of China. Published by Elsevier Ltd & Science Press

This is an open access article under the CC BY-NC-ND license (<http://creativecommons.org/licenses/by-nc-nd/4.0/>)

point Al_2Ca phase, which increased the ignition temperature to $662.5\text{ }^\circ\text{C}$. In addition, previous studies show that alloying with reactive elements [11], such as Be [12–15], Ca [15–17], and RE [10,13,18–23], can significantly improve the ignition temperature of Mg alloy, due to the formation of dense oxide film. However, most of these findings were obtained in the melt during a casting-like process, which resulted in relatively high ignition temperature due to the absent influence of external flame. Some studies [20–23] also acquired the corresponding ignition temperature or ignition delay time by placing the solid Mg alloy samples in a furnace for continuous heating tests or isothermal tests. However, they are distinct from the ignition of Mg alloy components. For aerospace applications, the primary concern is the flammability and ignition resistance of Mg components heated externally [21], that is, the ignition and combustion behaviors of Mg alloy components in the presence of flame. Besides, the research on the ignition characteristics of Mg alloys is relatively comprehensive, while the understanding of the combustion characteristics of Mg alloy components, especially about the flame spread resistance, is relatively insufficient.

Dimension is not only an important factor affecting the flame spread resistance of Mg alloy components, but also an indispensable part of fire-resistant design. However, the mechanism of the effect of sample dimension on flame spread is still unclear, and previous studies have mostly focused on the effects on ignition characteristics [23–25]. Therefore, there is an urgent need for researches on

how sample dimension affects flame spread, as well as criteria to guide the dimensional design of Mg alloy components. The purpose of the present work is to propose a criterion based on the combustion process of Mg alloys, which can predict the flame spread time and provide an index to guide the dimensional design of Mg alloy components. The accuracy and guiding significance of this criterion were verified by investigating the flame spread time of three Mg alloys of AZ80 (known as ZM5 in China), EZ30K (known as ZM6 in China) and WE43 with different sample dimensions.

2 Criterion and index for guiding dimensional design

Figure 1 shows the fire process of a stick-shaped Mg alloy sample. As shown in Figs. 1(a, b), the lowest end of the sample is heated by an external flame. Once the heated end is ignited, as shown in Fig. 1(c), the external flame is removed. The ignited area then oxidizes violently to burst out a flame with an initially stable height of δ_f , as shown in Fig. 1(d), which heats and ignites the remaining sample to maintain combustion. As shown in Fig. 1(e), Ω is a micro-region selected as the control volume, whose position is mobile and is always δ_f from the latest ignition point when used as the starting point of a study cycle. T_0 is the initial temperature of Ω when the heated end of the sample is ignited, as shown in Fig. 1(d), and T_{ig} is the ignition temperature. Although the flame becomes larger as the sample burns, the flame spread of a

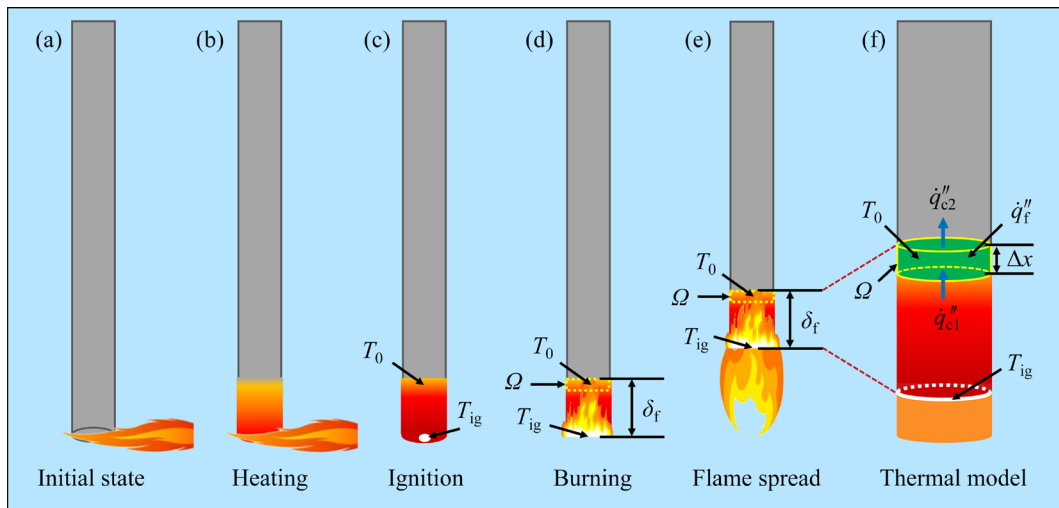


Fig. 1 Schematic diagrams of fire process of stick-shaped Mg alloy sample heated by external flame: (a) Initial state; (b) Heating; (c) Ignition; (d) Burning; (e) Flame spread; (f) Thermal model for flame spread

sample can actually be divided into the flame spread of each part, all of which are equivalent to parts with a height of δ_f being continuously heated and ignited by a similar initial flame. And the time it takes for the flame to heat and ignite Ω region is the time (t_f) required for the flame to spread the distance of δ_f .

QUINTIERE [26] proposed a criterion to predict the surface flame spread speed of solids such as wood. However, this criterion does not consider the effects of solid melting and sample dimension in detail, so it could not be directly employed to predict the combustion process of Mg alloy samples. Based on QUINTIERE's criterion, a thermal model was proposed to establish a criterion to predict the flame spread time of stick-shaped Mg alloy samples. Considering that the surface of the control volume Ω region is heated by the flame, it dissipates little and negligible heat to the ambient. As shown in Fig. 1(f), there are mainly three heat fluxes acting on the Ω region: \dot{q}_{c1}'' (heat flux per unit area of conduction from the ignited end), \dot{q}_{c2}'' (heat flux per unit area of conduction from Ω to the unignited end), and \dot{q}_f'' (average heat flux per unit area of the flame incident convection and radiation during Ω being heated from T_0 to T_{ig}). Since the temperatures and temperature gradients at different locations in the micro Ω region are almost the same, \dot{q}_{c1}'' is approximately equal to \dot{q}_{c2}'' . Therefore, the energy conservation equation in the process of Ω being heated from T_0 to T_{ig} without considering the relatively little evaporation is as follows:

$$\Delta x S \rho \Delta H = \Delta x l_c \dot{q}_f'' t_f \quad (1)$$

where Δx is the height of Ω region; S is the cross-sectional area of the sample; ρ is the density of the alloy; ΔH is the energy required to heat a unit mass of sample from T_0 to T_{ig} , and it is determined by the alloy material; l_c is the circumference of the cross section. The flame spread time t can be expressed as

$$t = \frac{L}{\delta_f} t_f = \frac{\Delta x S}{\Delta x l_c} \frac{L \rho \Delta H}{\delta_f \dot{q}_f''} = C \frac{\Delta x S}{\Delta x l_c} \quad (2)$$

where L is the length of the stick-shaped Mg alloy sample; C is defined as $\frac{L \rho \Delta H}{\delta_f \dot{q}_f''}$. In the same test condition, for samples with the same dimension, the flame spread time is almost proportional to ΔH ; for

samples with a certain length L , a certain volume and a certain Mg alloy material, C is almost constant and the flame spread time is determined by the shape of its cross-section. As for the control volume Ω , $\Delta x S$ is the volume heated by the flame, and $\Delta x l_c$ is the area of the surface receiving heat from the flame. Therefore, the flame spread time is proportional to the heated volume/receiving area ratio, that is,

$$t = C \frac{\Delta x S}{\Delta x l_c} = C \frac{S}{l_c} \quad (3)$$

The index of S/l_c ratio can guide the dimensional design of Mg alloy components. For stick-shaped samples with constant length and cross-sectional area, the sample with circular cross-section has the largest S/l_c ratio, indicating that its flame spread resistance is the best.

3 Experimental

3.1 Materials

The materials used to verify the criterion, three Mg alloys of ZM5, ZM6 and WE43, were prepared in as-extruded condition. Commercially pure Mg, Al and Zn, Mg–30Y, Mg–30Nd, Mg–30Zr and Mg–4Mn master alloys were used to prepare the ZM5, ZM6 and WE43 alloys. They were melted in an electric resistance furnace at 720 °C under the protection of CO₂ + SF₆ mixed gas, and then cast as semi-continuous cast rods with a diameter of 240 mm, at a casting speed of 30 mm/s. Three kinds of semi-continuous cast Mg alloy rods were solution-treated (ZM5: 375 °C for 24 h; ZM6 and WE43: 500 °C for 24 h) and extruded (ZM5: 350 °C; ZM6 and WE43: 450 °C) into plates (14.8 mm × 325 mm), with an extrusion speed of 5 mm/s and an extrusion ratio of approximately 9.4. The chemical compositions of the extruded plates were determined by inductively coupled plasma-atomic emission spectroscopy (ICP-AES) and listed in Table 1.

Table 1 Chemical compositions of three Mg alloys (wt.%)

Alloy	Al	Zn	Mn	Nd	Y	Zr	Mg
ZM5	8.5	0.5	0.2	–	–	–	Bal.
ZM6	–	0.4	–	2.7	–	0.6	Bal.
WE43	–	–	–	3.3	4.0	0.5	Bal.

3.2 Flame spread combustion test

Four kinds of samples with different dimensions were cut from each kind of Mg alloy extruded plate along the extrusion direction for the combustion test, which are $3\text{ mm} \times 20\text{ mm} \times 100\text{ mm}$, $5\text{ mm} \times 12\text{ mm} \times 100\text{ mm}$, $7.75\text{ mm} \times 7.75\text{ mm} \times 100\text{ mm}$ and $d8.74\text{ mm} \times 100\text{ mm}$ ($60\text{ mm}^2 \times 100\text{ mm}$). And the corresponding S/l_c ratios are 1.30, 1.76, 1.94, and 2.19 mm. As shown in Fig. 2, the samples were fixed on the crossbeams vertically and horizontally, respectively. The horizontal sample has the same ignition behavior as the vertical sample, since it is just rotated by 90° relative to the vertical sample in space as shown in Fig. 2. Since the burning flame is always vertical, the T_{ig} measured by the vertical sample will have a large deviation due to the influence of the flame, while this deviation can be eliminated in the horizontal sample. Therefore, the horizontal sample was used to obtain the parameters of T_0 and T_{ig} needed to predict the flame spread time t of the vertical sample. Ω is a micro-region on the sample and 15 mm away from the heated end, which is approximately the height of the flame at which Mg alloy sample initially burns. A K-type thermocouple, connected to a data-acquisition system that generates ten readings per second, was fixed at Ω region and used to record its initial temperature T_0 and ignition temperature T_{ig} . The sample was heated by the butane gun with a heat flux of approximately 191 kW/m^2 , and the butane gun was rapidly removed once the sample was ignited. For each dimension of the alloy, the T_0 and T_{ig} were the averages of five tests, while the flame spread time t was the average of ten tests. As shown in Fig. 2, the

average heat flux \dot{q}_f'' was measured by a heat flux sensor (CAPTEC, GD-B3-200K) and recorded by a data recorder (CAPTEC, HFM-8).

3.3 Characterization

The microstructures of alloys before and after combustion tests were observed by an optical microscope (OM, Zeiss Axio Observer A1). The specimens for metallographic observation and phase identification were cut from the extruded plates and the extinguished samples longitudinally. The metallographic specimens were ground, polished and etched with 4% HNO_3 for 8 s before characterization. The specimens were ground before identifying phases by Rigaku X-ray diffraction with a $\text{Cu K}\alpha_1$ radiation source, a scanning speed of $2^\circ/\text{min}$, a voltage of 40 kV and a current of 30 mA. The density of each alloy was obtained from an electronic balance (Sartorius Quintix124-1CN) with a densimeter (YDK03P), using the Archimedes method.

4 Results and discussion

4.1 Ignition and combustion behavior

As shown in Fig. 3(a), the state of the ZM5 alloy sample with a dimension of $3\text{ mm} \times 20\text{ mm} \times 100\text{ mm}$ during the fire process mainly includes: oxidation, melting, ignition, spreading and dropping. As shown in Fig. 3(a), in the ZM5 alloy sample, when the heating time was 10 s, the heated area turned gray, which was a typical phenomenon of oxidation. When the heating time was 37 s, some solids were melted into liquids and pooled to form a bulge at the lowest end of the sample. Under the

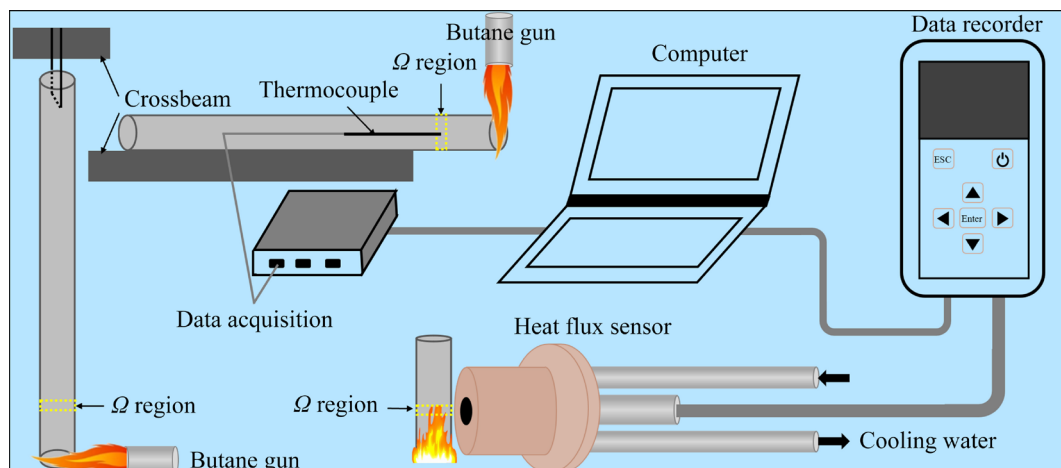


Fig. 2 Schematic diagram of combustion test



Fig. 3 Fire progresses of ZM5 (a), ZM6 (b) and WE43 (c) Mg alloy samples with dimension of 3 mm × 20 mm × 100 mm

influence of gravity, the ZM5 sample was easily deformed due to the low flow stress at high temperatures [27,28], causing the oxide film to rupture. Then, the Mg vapor escaped and was ignited, where the yellow flame was the direct evidence of the combustion of Mg vapor. When the ZM5 sample was ignited, the melted part locally dropped off. Then, the flame stabilized and began to heat the remaining unignited part. When the remaining part was all ignited, the sample dropped, that is, the flame spread ended at 145 s, as shown in Fig. 3(a). Therefore, the flame spread time t of this ZM5 alloy sample is 101 s.

As shown in Figs. 3(b, c), the fire processes of the ZM6 and WE43 Mg alloy samples are basically similar to those of the ZM5 alloy sample. However, there is no obvious deformation and local dropping

like the ZM5 sample, because Mg–RE alloys have better high-temperature mechanical properties. In addition, the ignition time of the ZM6 sample is longer than that of the ZM5 sample, and that of the WE43 sample is the longest, which are all associated with their dense oxide films [5,6,12,29]. As shown in Figs. 3(b, c), the flame spread time values of the ZM6 and WE43 alloy samples with a dimension of 3 mm × 20 mm × 100 mm are 97 and 63 s, respectively.

Figure 4 shows the temperature curves of the three horizontally placed Mg alloy samples with a dimension of 3 mm × 20 mm × 100 mm. It can be seen that the ignition time values of the samples are basically the same as those of the vertically fixed samples shown in Fig. 3, which verifies that the horizontal samples have the same ignition behavior

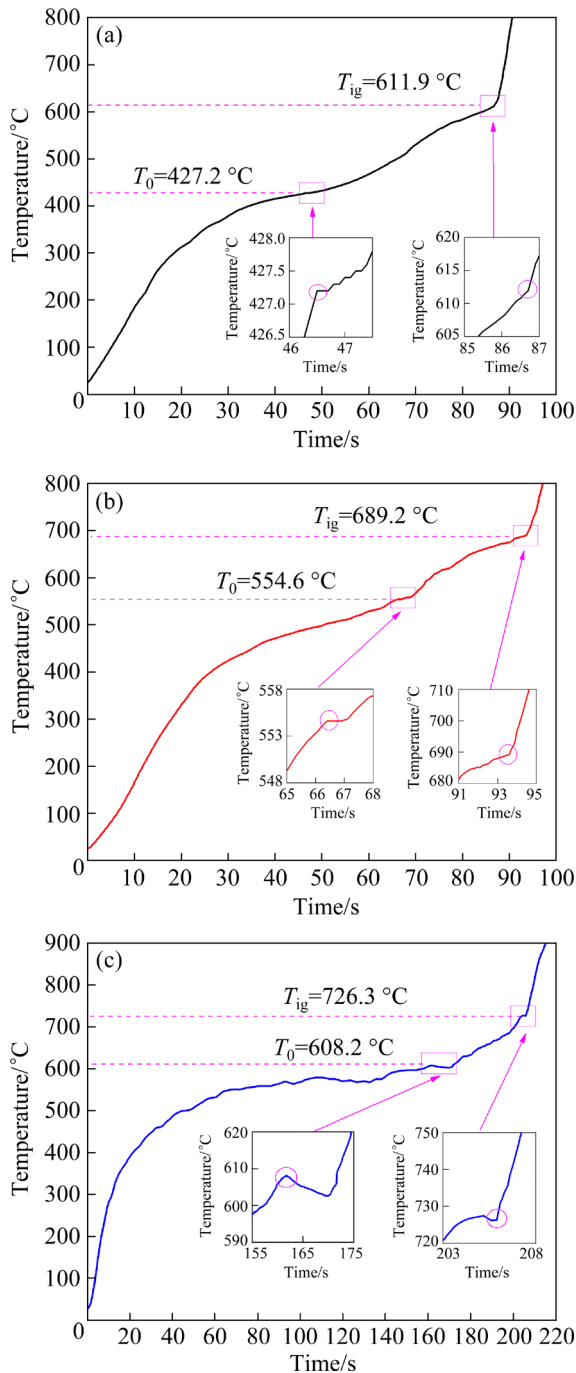


Fig. 4 Temperature–time curves of Ω regions on horizontal ZM5 (a), ZM6 (b) and WE43 (c) Mg alloy samples with dimension of 3 mm \times 20 mm \times 100 mm

as the vertical samples. As shown in Fig. 4(a), in the ZM5 alloy sample, the temperature of the Ω region increases rapidly within 30 s, mainly because the heated end was still in the solid state at this time, and a lot of heat was conducted to the Ω region. As shown in Fig. 3(a), the heated end was in the melting stage at 37 s, which needed to absorb a lot of heat, so most of the heat was used to melt solid instead of being conducted to the Ω region.

Therefore, the temperature of the Ω region increased slowly during 35–45 s. Since the heat source was removed when ignition, the increase of temperature significantly slowed for a short period of time. As shown in Fig. 4(a), when the heated end of the horizontal sample was ignited, the initial temperature T_0 of the ZM5 alloy sample with a dimension of 3 mm \times 20 mm \times 100 mm was 427.2 °C. Generally, the ignition releases a lot of heat and causes the temperature to rise sharply, so the inflection point of the temperature curve is the ignition temperature [7]. Therefore, as shown in Fig. 4(a), the corresponding ignition temperature T_{ig} of the ZM5 alloy sample with a dimension of 3 mm \times 20 mm \times 100 mm is 611.9 °C. Similarly, as shown in Figs. 4(b, c), the initial temperatures T_0 and ignition temperatures T_{ig} of the ZM6 and WE43 alloy samples with a dimension of 3 mm \times 20 mm \times 100 mm are 554.6 and 608.2 °C, 689.2 and 726.3 °C, respectively.

As shown in Fig. 5, some samples with dimensions of 7.75 mm \times 7.75 mm \times 100 mm and ϕ 8.74 mm \times 100 mm were extinguished during the combustion process, which achieved the purpose of improving the flame spread resistance through dimensional design. As shown in Figs. 5(a–c), the flame of the sample with circular cross section is difficult to ignite the remaining part, which causes it easy to extinguish. In addition, if the semi-solid or liquid part is not ignited by the flame in time, it will drop and take away a lot of heat, making it easier for the sample to extinguish. The dropping phenomenon is common in the ZM5 alloy samples. As shown in Fig. 5(d), the flames of four 7.75 mm \times 7.75 mm \times 100 mm and four ϕ 8.74 mm \times 100 mm ZM5 alloy samples extinguished during their combustion processes. As shown in Figs. 5(e, f), the same phenomenon is also observed in the ZM6 and WE43 samples. It is clear that the flame spread resistance of the sample with circular cross-section is the best due to the largest S/l_c ratio.

4.2 Microstructure affecting initial temperature and ignition temperature

The phase stability affects the ignition temperature, and usually, a high ignition temperature is associated with high solidus and liquidus of the alloy and high melting point secondary phase [6]. As shown in Figs. 6(a–c), the microstructures of the as-extruded ZM5, ZM6 and

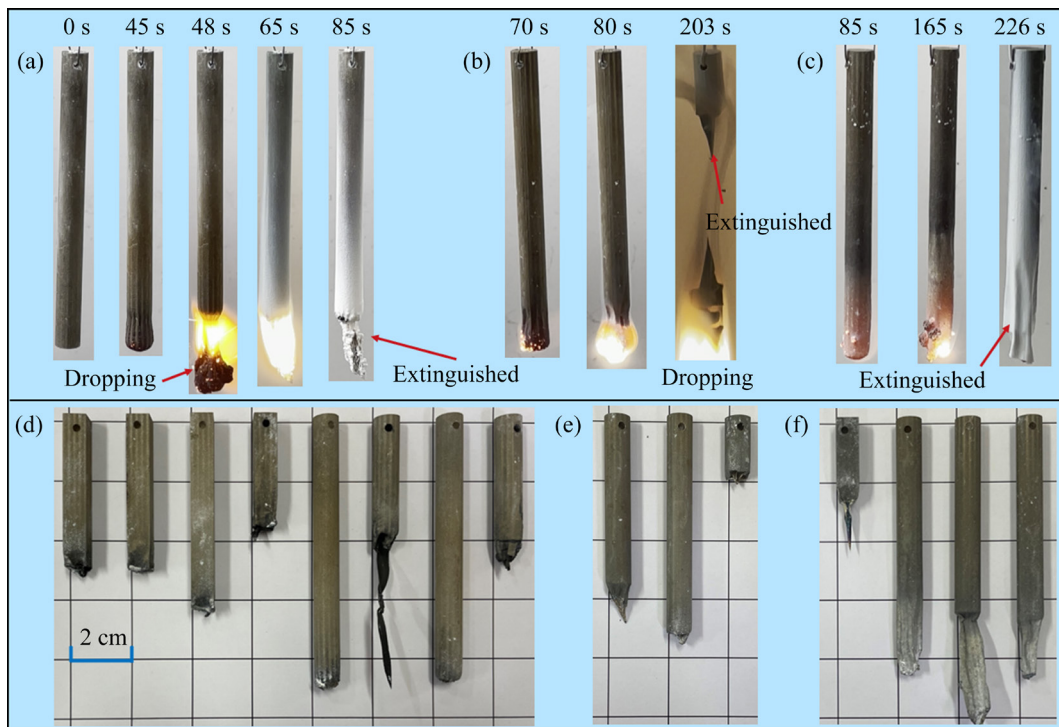


Fig. 5 Fire extinguishing processes of ZM5 (a), ZM6 (b) and WE43 (c) alloy samples with dimension of $d8.74 \text{ mm} \times 100 \text{ mm}$, and ZM5 (d), ZM6 (e) and WE43 (f) samples extinguished during combustion progress

WE43 alloys consist of equiaxed α -Mg grains and some secondary phases, and the diameters of most grains are between $50 \mu\text{m}$ and $100 \mu\text{m}$. According to the solidification path shown in Fig. 6(d) calculated by JMatPro 7.0 software based on the Scheil's model, both the solidus and liquidus of the ZM5 alloy are low, which explains its lowest ignition temperature. The Al_8Mn_5 phase is formed before the α -Mg, which mainly acts as the heterogeneous nucleation substrate for α -Mg. Therefore, the Al_8Mn_5 particles are usually small and locate inside the α -Mg grains. The $\text{Mg}_{17}\text{Al}_{12}$ phase generates after the α -Mg and it usually distributes along the grain boundary. Some of the $\text{Mg}_{17}\text{Al}_{12}$ was decomposed and dissolved into the Mg matrix during solution treatment, so only part of $\text{Mg}_{17}\text{Al}_{12}$ remained in the as-extruded microstructure, as shown in Fig. 6(a). As shown in Fig. 7, according to the XRD results, there are indeed some $\text{Mg}_{17}\text{Al}_{12}$ particles remaining in the as-extruded microstructure of the ZM5 alloy, while the Al_8Mn_5 is too little to be detected. Since the melting point of the $\text{Mg}_{17}\text{Al}_{12}$ phase is only $463.3 \text{ }^\circ\text{C}$, its thermal instability is also a factor leading to the low ignition temperature of the ZM5 alloy. As shown in Figs. 6 and 7, the situation in the ZM6 and WE43 Mg

alloys is similar to that of the ZM5 alloy, except that their solidus and liquidus are higher, and their secondary phases are more stable. Similarly, the Zr phase is too little to be detected. The fractions of the secondary phases in the as-extruded microstructures are smaller than those predicted by the nonequilibrium solidification paths due to the solution treatment, but the types of secondary phases did not change according to the XRD results shown in Fig. 7.

As shown in Fig. 4(a), the initial temperature T_0 of ZM5 alloy sample is only $427.2 \text{ }^\circ\text{C}$, which is related to its low solidus affected by the low melting point $\text{Mg}_{17}\text{Al}_{12}$ phase. Since a lot of heat is required in the melting process, the temperature of the Ω region will stay near the solidus for a long time, which makes the temperature rise slowly when the heated end is ignited. Similarly, the initial temperature T_0 of the ZM6 alloy sample is close to its solidus temperature of $553.2 \text{ }^\circ\text{C}$. Differently, the ignition time of the WE43 alloy was much longer, so more energy was provided to increase the temperature of the Ω region, resulting in a significantly higher initial temperature. In addition, the low ignition temperature of the ZM5 alloy is associated with its low liquidus. As shown in

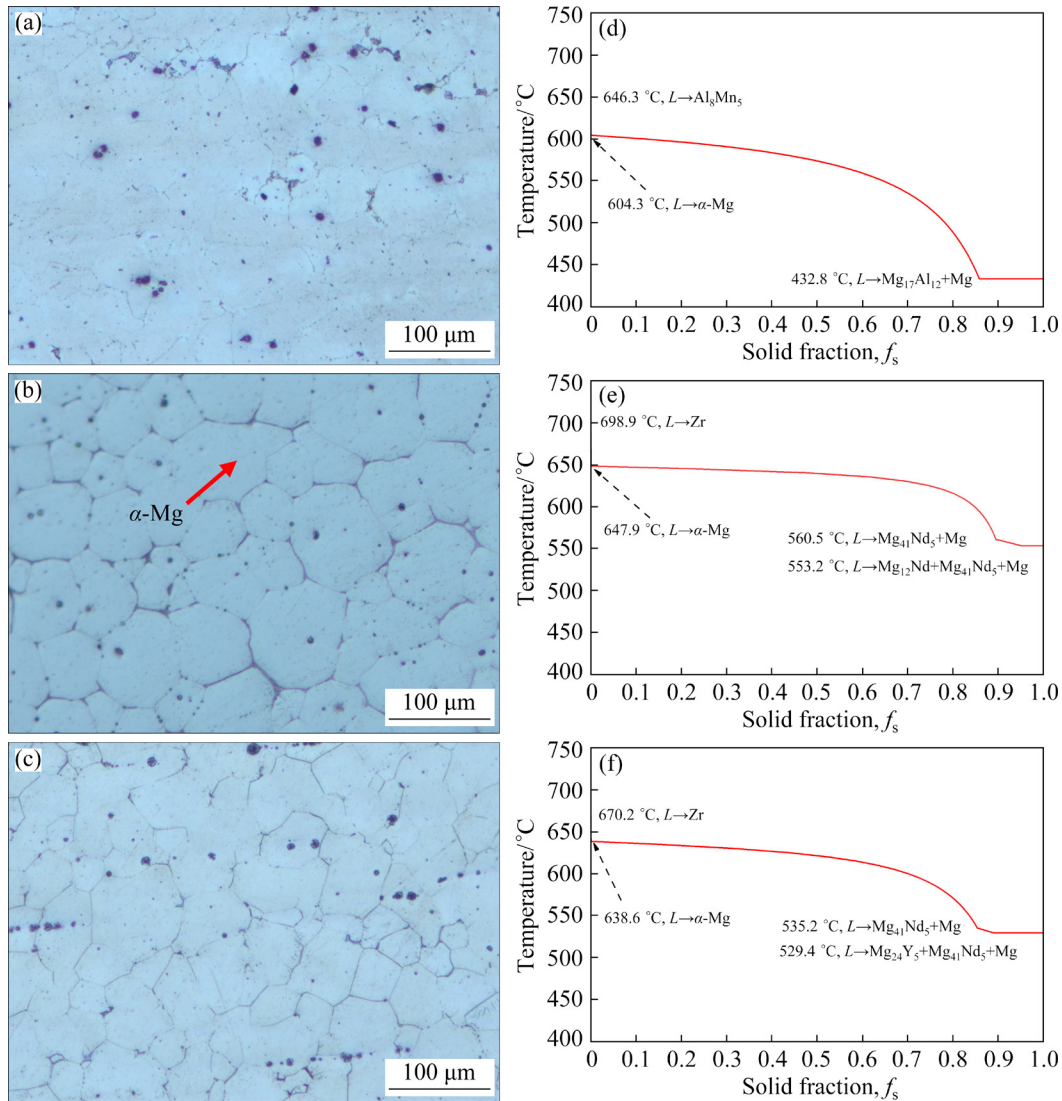


Fig. 6 Microstructures of ZM5 (a), ZM6 (b) and WE43 (c) alloys before combustion test, and nonequilibrium solidification paths of ZM5 (d), ZM6 (e) and WE43 (f) alloys calculated by JMatPro 7.0 software based on Scheil's model

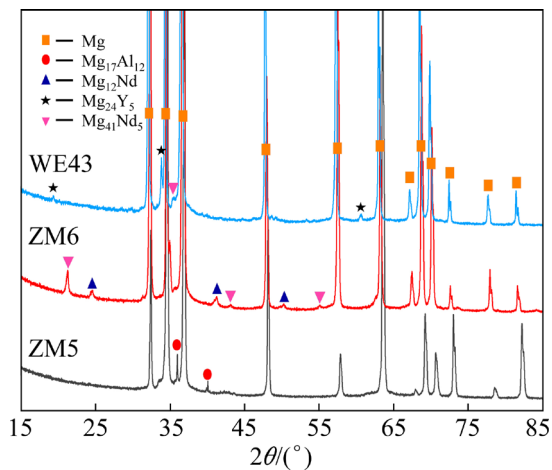


Fig. 7 XRD patterns of as-extruded ZM5, ZM6 and WE43 Mg alloys

Figs. 4(a) and 6(d), the ignition temperature of 611.9 °C is close to the liquidus of 604.3 °C. Due to the low flow stress at high temperatures [27,28], the ZM5 alloy sample is easy to deform and drop after melting. Therefore, when the temperature approaches the liquidus, the Mg vapor will escape from the ruptured oxide film and be ignited. Differently, the ZM6 and WE43 alloys have higher liquidus temperatures and denser oxide films [7,11,30], so they need more Mg vapor to rupture the oxide film and cause ignition, which results in higher ignition temperatures.

4.3 Microstructure evolution

Figure 8 shows the microstructures of the

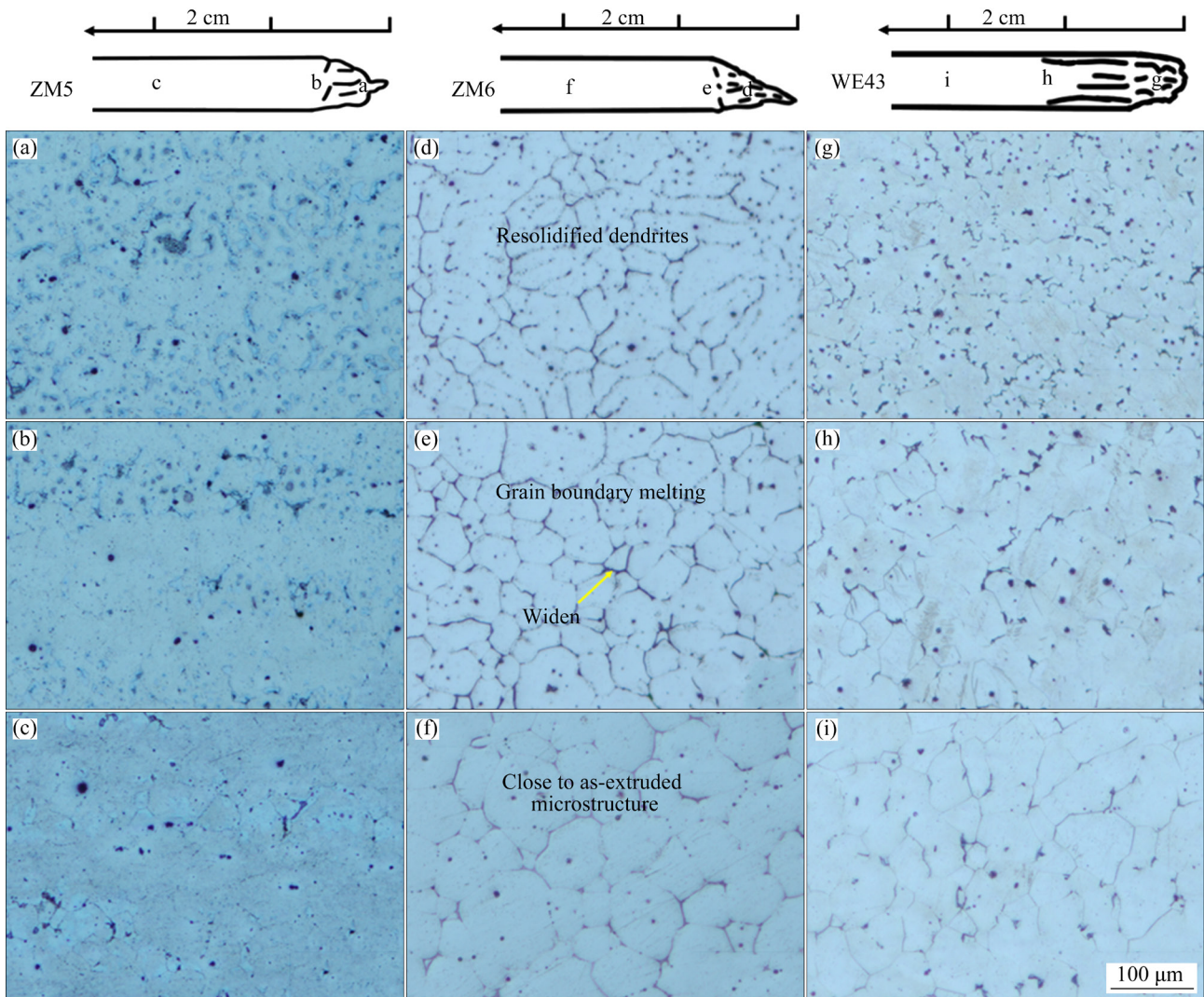


Fig. 8 Microstructures of extinguished ZM5 (a–c), ZM6 (d–f) and WE43 (g–i) alloy samples with dimension of $\phi 8.74 \text{ mm} \times 100 \text{ mm}$ at different locations

extinguished samples at different positions, which are used to understand the evolution of the microstructure during combustion. As shown in Figs. 8(a, d, g), microstructures of extinguished ends of the three Mg alloy samples are typical nonequilibrium solidification microstructures, which are mainly composed of dendritic α -Mg matrix and intergranular secondary phases. Since the extinguished end was heated to liquid state by the flame and then resolidified to solid state, its microstructure is consistent with that predicted by the solidification path shown in Fig. 6. According to the XRD results shown in Fig. 9, the main secondary phase in the ZM5 alloy is $\text{Mg}_{17}\text{Al}_{12}$, while the Al_8Mn_5 phase is difficult to be detected due to its low fraction. In the ZM6 alloy, the main secondary phases are Mg_{12}Nd and $\text{Mg}_{41}\text{Nd}_5$.

In the WE43 alloy, the main secondary phases are Mg_{24}Y_5 and $\text{Mg}_{41}\text{Nd}_5$. Similarly, the Zr phase in the ZM6 and WE43 alloys is too little to be detected.

As shown in Figs. 8(b, e, h), there is a typical overheating phenomenon in the microstructures at the edge of the deformed areas of the Mg alloy samples, that is, the widened grain boundary. Under the heating of the flame, the grain boundary was melted first due to the enrichment of solutes or low-melting secondary phases, and the liquid resolidified and led to the widened grain boundary after the flame was extinguished. As for the microstructures away from the extinguished ends, as shown in Figs. 8(c, f, i), they are less affected by the flame and basically the same as the original as-extruded microstructures.

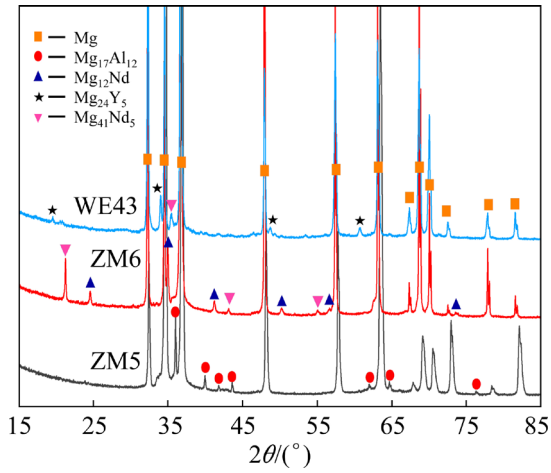


Fig. 9 XRD results of resolidified microstructures in extinguished ends of ZM5, ZM6 and WE43 alloy samples

4.4 Validation of criterion

The T_0 , T_{ig} and t of all samples were obtained and presented in Tables 2 and 3, where only unextinguished samples were considered when calculating the average flame spread time. It should be noted that, the combustion behaviors of the three Mg alloys in the present work are basically the same. Therefore, T_0 and T_{ig} values measured for each alloy are basically the same, and then the average values were used for discussion; in addition, the measured \dot{q}_f'' and δ_f values for three Mg alloy samples are very close, approximately 85 kW/m² and 15 mm, respectively. As shown in Table 2, due to the large temperature difference between T_0 and T_{ig} , the ΔH value of the ZM5 alloy is the largest, which results in the largest C value. Therefore, as for samples with the same dimension, the ZM5 alloy has the longest flame spread time, as given in Table 3.

As shown in Fig. 10(a), enthalpy–temperature curves were calculated by JMatPro 7.0 software to obtain the ΔH . Figure 10(b) indicates that the sample with circular cross-section has the largest S/l_c ratio and the largest flame spread time for each

Table 2 Parameters for predicting flame spread time

Alloy	ρ/l (g·cm ⁻³)	$T_0/^\circ\text{C}$	$T_{ig}/^\circ\text{C}$	$\Delta H/$ (J·g ⁻¹)	$C/$ (s·mm ⁻¹)
ZM5	1.795	427.9	613.9	520.2	73.2
ZM6	1.781	556.5	687.6	477.8	66.7
WE43	1.813	610.1	729.9	342.9	48.8

Table 3 S/l_c value and average flame spread time t for each sample

Dimension	$(S/l_c)/$ mm	t/s		
		ZM5	ZM6	WE43
3 mm × 20 mm × 100 mm	1.30	98	95	63
5 mm × 12 mm × 100 mm	1.76	124	115	85
7.75 mm × 7.75 mm × 100 mm	1.94	145	136	103
$d8.74$ mm × 100 mm	2.19	156	144	116

Mg alloy. In addition, since the WE43 alloy has the best ignition-proof resistance [7], its ignition time is the longest, as shown in Figs. 3(c) and 4(c), which leads to the highest initial temperature T_0 , the smallest C value, and the shortest flame spread time t . As shown in Fig. 10(c), the flame spread time t has a good proportional relationship with the S/l_c ratio, which is consistent with the predictions. As shown in Figs. 10(d–f), the measured values of the flame spread time are close to the predicted values, and the errors are within 10%. Therefore, for different Mg alloys, the difference is mainly reflected in the C value; for samples of the same alloy, the difference is mainly reflected in the S/l_c ratio. Compared with the sample with a dimension of 3 mm × 20 mm × 100 mm, through the dimensional optimization, the flame spread time values of the ZM5, ZM6 and WE43 samples with a dimension of $d8.74$ mm × 100 mm were delayed by 59.2%, 51.6% and 84.1%, respectively, and even the effect of flame extinguishing was achieved.

5 Conclusions

(1) This criterion indicates that the flame spread time of Mg alloys is mainly related to the material and sample dimension: the material affects the ΔH , and the sample dimension determines the S/l_c ratio.

(2) The initial temperature and ignition temperature of the ZM5 alloy are much lower than those of the ZM6 and WE43 alloys, due to its low solidus and liquidus.

(3) The sample with circular cross-section has better flame spread resistance than that with rectangular cross-section. Under the guidance of this criterion, it is possible to delay the flame spread time by at least 51.6% and even extinguish the flame through dimensional optimization.

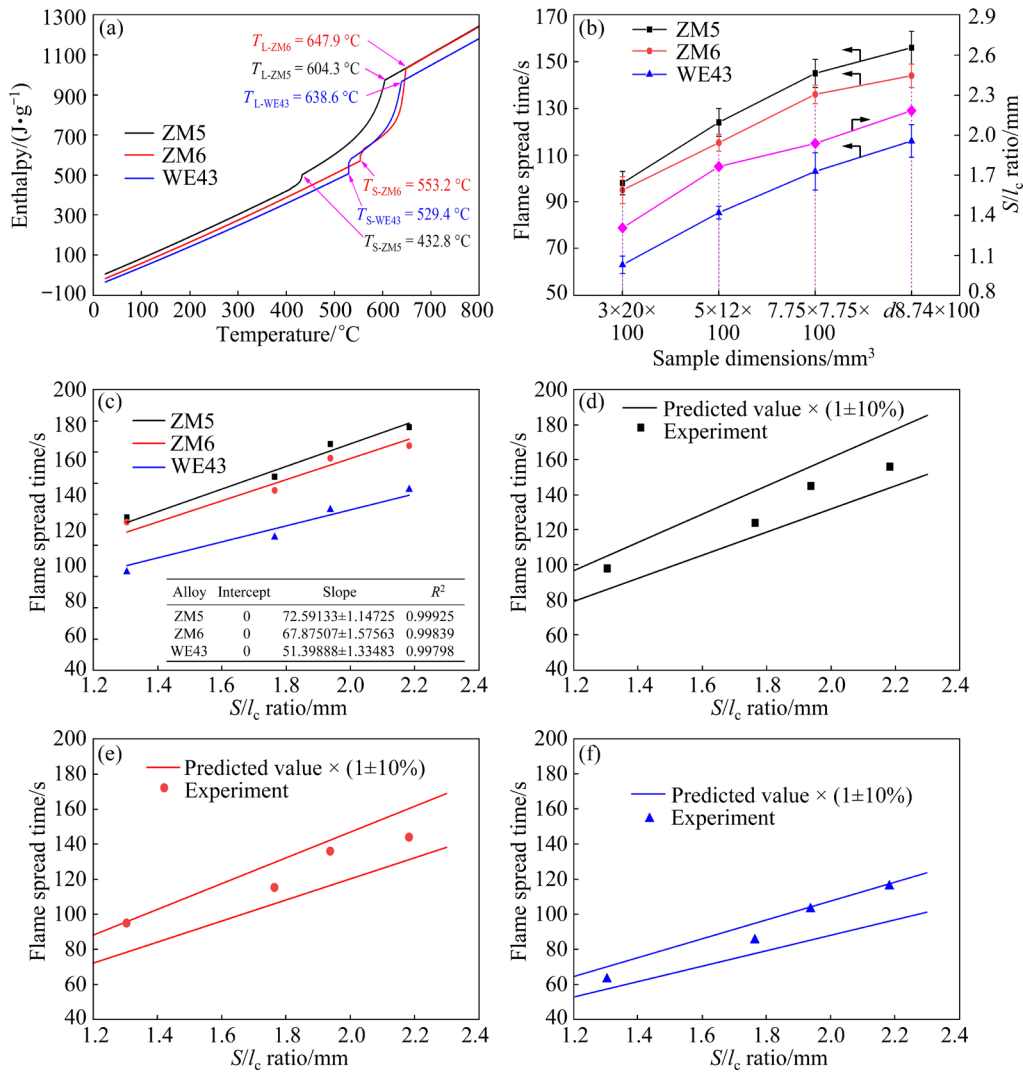


Fig. 10 Enthalpy–temperature curves calculated by JMatPro 7.0 software (a); Average flame spread time and S/l_c ratio for each sample (b); Average flame spread time versus S/l_c ratio curves (c); Errors of average flame spread time between predicted and experimental values in ZM5 (d), ZM6 (e) and WE43 (f) alloys

CRedit authorship contribution statement

Bo HU: Writing – Original draft, Conceptualization, Data curation, Methodology, Validation, Investigation, Formal analysis, Visualization; **Jia-xuan HAN:** Data curation, Methodology, Validation, Investigation, Formal analysis, Visualization; **De-jiang LI:** Writing – Review & editing, Conceptualization, Supervision, Project administration, Funding acquisition; **Zi-xin LI:** Investigation, Formal analysis; **Xiao-qin ZENG** and **Wen-jiang DING:** Supervision, Project administration, Funding acquisition; **Zhan-hong LIN, Chen JIN** and **Shou ZHAO:** Investigation, Project administration.

Declaration of competing interest

The authors declare that they have no known competing financial interests or personal relationships

that could have appeared to influence the work reported in this paper.

Acknowledgments

This work was supported by the National Key Research and Development Program of China (No. 2021YFB3501002), the National Science and Technology Major Project of China (No. J2019-VIII-0003-0165), and Qinghai Salt Lake Industry Co., Ltd. financially by the Science and Technology Project, China (No. 21-ZC0609-0003).

References

[1] FAKHAR N, SABBAGHIAN M. Hot shear deformation constitutive analysis of fine-grained ZK60 Mg alloy sheet

- fabricated via dual equal channel lateral extrusion and sheet extrusion [J]. Transactions of Nonferrous Metals Society of China, 2022, 32(8): 2541–2556.
- [2] GUO Kun-yu, XU Chang, LIN Xiao-ping, YE Jie, ZHANG Chong, HUANG Duo. Microstructure and strengthening mechanism of Mg–5.88Zn–0.53Cu–0.16Zr alloy solidified under high pressure [J]. Transactions of Nonferrous Metals Society of China, 2020, 30(1): 99–109.
- [3] HOU Ying-ying, WU Meng-wu, TIAN Bing-hui, LI Xiao-bo, XIONG Shou-mei. Characteristics and formation mechanisms of defect bands in vacuum-assisted high-pressure die casting AE44 alloy [J]. Transactions of Nonferrous Metals Society of China, 2022, 32(6): 1852–1865.
- [4] ZHANG Wan-peng, MA Ming-long, YUAN Jia-wei, SHI Guo-liang, LI Yong-jun, LI Xing-gang, ZHANG Kui. Microstructure and thermophysical properties of Mg–2Zn–xCu alloys [J]. Transactions of Nonferrous Metals Society of China, 2020, 30(7): 1803–1805.
- [5] CZERWINSKI F. Controlling the ignition and flammability of magnesium for aerospace applications [J]. Corrosion Science, 2014, 86: 1–16.
- [6] TEKUMALLA S, GUPTA M. An insight into ignition factors and mechanisms of magnesium based materials: A review [J]. Materials & Design, 2017, 113: 84–98.
- [7] HAN Dong, ZHANG Jin, HUANG Jin-feng, LIAN Yong, HE Guang-yu. A review on ignition mechanisms and characteristics of magnesium alloys [J]. Journal of Magnesium and Alloys, 2020, 8: 329–344.
- [8] TIMOTHY M. Evaluating the flammability of various magnesium alloys during laboratory- and full-scale aircraft fire tests [R]. Department of Transportation, Federal Aviation Administration, Atlantic City, New Jersey, 2013.
- [9] TAN X H, HOW W C K, WENG J C K, ONN R K W, GUPTA M. Development of high-performance quaternary LPSO Mg–Y–Zn–Al alloys by disintegrated melt deposition technique [J]. Materials & Design, 2015, 83: 443–450.
- [10] CHENG Chun-long, LAN Qing, LIAO Qi-yu, LE Qi-chi, LI Xiao-qiang, CHEN Xing-rui, CUI Jian-zhong. Effect of Ca and Gd combined addition on ignition temperature and oxidation resistance of AZ80 [J]. Corrosion Science, 2019, 160: 108176.
- [11] TAN Qi-yang, YIN Yu, MO Ning, ZHANG Ming-xing, ATRENS A. Recent understanding of the oxidation and burning of magnesium alloys [J]. Surface Innovations, 2019, 7(2): 71–92.
- [12] TAN Qi-yang, MO Ning, LIN Chih-ling, JIANG Bin, PAN Fu-sheng, HUANG Han, ATRENS A, ZHANG Ming-xing. Improved oxidation resistance of Mg–9Al–1Zn alloy microalloyed with 60 wt ppm Be attributed to the formation of a more protective (Mg,Be)O surface oxide [J]. Corrosion Science, 2018, 132: 272–283.
- [13] ZENG Xiao-qin, WANG Qu-dong, LU Yi-zhen, ZHU Yan-ping, DING Wen-jiang, ZHAO Yun-hu. Influence of beryllium and rare earth additions on ignition-proof magnesium alloys [J]. Journal of Materials Processing and Technology, 2001, 112(1): 17–23.
- [14] ZENG Xiao-qin, WANG Qu-dong, LU Yi-zhen, DING Wen-jiang, ZHU Yan-ping, ZHAI Chun-quan, LU Chen, XU Xiao-ping. Behavior of surface oxidation on molten Mg–9Al–0.5Zn–0.3Be alloy [J]. Materials Science and Engineering A, 2001, 301(2): 154–161.
- [15] INOUE S I, YAMASAKI M, KAWAMURA Y. Oxidation behavior and incombustibility of molten Mg–Zn–Y alloys with Ca and Be addition [J]. Corrosion Science, 2019, 149: 133–143.
- [16] LEE D B. High temperature oxidation of AZ31 + 0.3 wt.% Ca and AZ31 + 0.3 wt.% CaO magnesium alloys [J]. Corrosion Science, 2013, 70: 243–251.
- [17] INOUE S I, YAMASAKI M, KAWAMURA Y. Formation of an incombustible oxide film on a molten Mg–Al–Ca alloy [J]. Corrosion Science, 2017, 122: 118–122.
- [18] YIN Si-qi, DUAN Wen-chao, LIU Wen-hong, WU Liang, YU Jia-min, ZHAO Zi-long, LIU Min, WANG Ping, CUI Jian-zhong, ZHANG Zhi-qiang. Influence of specific second phases on corrosion behaviors of Mg–Zn–Gd–Zr alloys [J]. Corrosion Science, 2020, 166: 108419.
- [19] FAN J, YANG G C, ZHOU Y H, WEI Y H, XU B S. Selective oxidation and the third-element effect on the oxidation of Mg–Y alloys at high temperatures [J]. Metallurgical and Materials Transactions A, 2009, 40: 2184–2189.
- [20] LIN Peng-yu, ZHOU Hong, SUN Na, LI Wen-ping, WANG Cheng-tao, WANG Ming-xing, GUO Qing-chun, LI Wei. Influence of cerium addition on the resistance to oxidation of AM50 alloy prepared by rapid solidification [J]. Corrosion Science, 2010, 52: 416–421.
- [21] LIU M, SHIH D S, PARISH C, ATRENS A. The ignition temperature of Mg alloys WE43, AZ31 and AZ91 [J]. Corrosion Science, 2012, 54: 139–142.
- [22] CHENG Chun-long, LE Qi-chi, LI Duo-jiao, HU Wen-xin, WANG Tong, GUO Rui-zhen, HU Cheng-lu. Effect of Y on high-temperature oxidation behavior and products of AZ80 alloy [J]. Materials Chemistry and Physics, 2021, 269: 124732.
- [23] DVORSKY D, KUBASEK J, ROUDNICKA M, PRUSA F, NECAS D, MINARIK P, STRASKA J, VOJTECH D. The effect of powder size on the mechanical and corrosion properties and the ignition temperature of WE43 alloy prepared by spark plasma sintering [J]. Journal of Magnesium and Alloys, 2021, 9(4): 1349–1362.
- [24] TEKUMALLA S, GUPTA M, MIN K H. Using CaO nanoparticles to improve mechanical and ignition response of magnesium [J]. Current Nanomaterials, 2018, 3: 44–51.
- [25] HAN Guo-song, CHEN Ding, CHEN Gang, HUANG Jiang-hua. Development of non-flammable high strength extruded Mg–Al–Ca–Mn alloys with high Ca/Al ratio [J]. Journal of Materials Science and Technology, 2018, 34: 2063–2068.
- [26] QUINTIERE J G. Fundamentals of fire phenomena [M]. Chichester: John Wiley & Sons Ltd., 2006.
- [27] HUANG Ying-jie, ZENG Guang, HUANG Li-xin, ZHENG Ze-bang, LIU Chun-ming, ZHAN Hong-yi. Influence of strain rate on dynamic recrystallization behavior and hot formability of basal-textured AZ80 magnesium alloy [J]. Materials Characterization, 2022, 187: 111880.
- [28] CHEN Fei-teng, JIANG Shu-nong, CHEN Zhi-yong, LIU Chu-ming. Effects of heat treatment on microstructure and tensile properties of isothermal die forged AZ80–Ag casing

- with large size [J]. Transactions of Nonferrous Metals Society of China, 2023, 33(8): 2340–2350.
- [29] KUMAR N R, BLANDIN J, SUERRY M, GROSJEAN E. Effect of alloying elements on the ignition resistance of magnesium alloys [J]. Scripta Materialia, 2003, 49: 225–230.
- [30] INOUE S I, YAMASAKI M, KAWAMURA Y. Classification of high-temperature oxidation behavior of Mg–1at.%X binary alloys and application of proposed taxonomy to nonflammable multicomponent Mg alloys [J]. Corrosion Science, 2020, 174: 108858.

一种提高镁合金零部件抗火焰蔓延性的尺寸设计类判据

胡波¹, 韩嘉璇¹, 李德江¹, 李子昕¹, 曾小勤¹, 丁文江¹, 林占宏², 金晨², 赵寿²

1. 上海交通大学 材料科学与工程学院
轻合金精密成型国家工程研究中心&金属基复合材料国家重点实验室, 上海 200240;
2. 青海盐湖特立镁有限公司, 西宁 810000

摘要: 基于能量守恒定律提出了一种用于预测棒状镁合金样品火焰蔓延时间的判据, 该判据表明火焰蔓延时间主要受合金材料和样品尺寸影响。控制体的初始温度和起燃温度以及样品的 S/l_c 比值(样品横截面面积/横截面周长)是火焰蔓延时间的决定性因素。火焰蔓延时间正比于 ΔH (将单位质量的样品从初始温度加热到起燃温度所需的能量)和 S/l_c 比值, 这在 Mg–8.5Al–0.5Zn–0.2Mn、Mg–2.7Nd–0.4Zn–0.6Zr 和 Mg–4.0Y–3.3Nd–0.5Zr 镁合金中得到验证。对于尺寸相同的样品, Mg–8.5Al–0.5Zn–0.2Mn 合金样品有着最大的 ΔH 以及最长的火焰蔓延时间; 对于材质、长度和横截面面积相同的样品, 圆形横截面样品的 S/l_c 比值最大, 其抗火焰蔓延性能也最佳。

关键词: 镁合金零部件; 抗火焰蔓延性; 显微组织; 尺寸设计; 判据

(Edited by Bing YANG)